UC Davis
UC Davis Previously Published Works

Title

Lateral Thrust Distribution of Column-Supported Embankments for Limiting Cases of Lateral Spreading

Permalink

Journal

ISSN

Authors

Huang, Zhanyu
Ziotopoulou, Katerina
Filz, George M

Publication Date
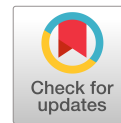
DOI

Peer reviewed

Lateral Thrust Distribution of Column-Supported Embankments for Limiting Cases of Lateral Spreading

Zhanyu Huang, A.M.ASCE[1]; Katerina Ziotopoulou, A.M.ASCE[2]; and George M. Filz, Dist.M.ASCE[3]

Abstract: Lateral spreading analysis of column-supported embankments (CSEs) requires an understanding of lateral thrust distribution. This includes quantifying the portion of thrust that is resisted by tension in geosynthetic reinforcements installed in the load transfer platform. Results from a three-dimensional (3D) numerical parametric study using a half-embankment domain and totaling 140 scenarios are presented in terms of lateral thrust distribution. Forces examined include the lateral thrusts in the embankment and foundation soil, the geosynthetic tension, and the base shear at depth, and results are presented for the limiting cases of lateral spreading (i.e., undrained end-of-construction and long-term dissipated). Results show that lateral thrusts induced by embankment loading are significant in the embankment, foundation soil, and base shear beneath the columns. However, the portion of lateral thrust carried by the geosynthetic is limited, though it increases with the geosynthetic stiffness. Results also indicate that lateral spreading in CSEs is more critical at the undrained end-of-construction condition than in the long-term condition after excess pore water pressures have dissipated. Correlations for the thrust distribution at these limiting conditions and different embankment locations (i.e., centerline, shoulder, and toe) are provided. **DOI: [10.1061/(ASCE)GT.1943-5606.0002375](https://doi.org/10.1061/(ASCE)GT.1943-5606.0002375).** © 2020 American Society of Civil Engineers.

Introduction

In projects where embankments need to be constructed, column-supported embankments (CSEs) are typically preferred when project success is controlled by time constraints. Unlike traditional methods of embankment construction on soft ground, such as staged fill placement with the use of prefabricated vertical drains, CSEs can be rapidly constructed without waiting for excess pore pressure dissipation. The benefit of accelerated construction derives from the transfer of embankment and service loading to a competent stratum at depth using foundation columns (CSE schematic illustrated in Fig. 1). Owing to differences in stiffness and settlement of the subsoil and columns, vertical loads are transferred to columns through soil arching in the embankment and friction on the column–soil interfaces. Often, a load transfer platform (LTP) is included at the embankment base. The shear strength of the LTP facilitates soil arching, and geosynthetic reinforcements may be included in the LTP as they can develop tension with vertical deflection and transfer additional loading to columns. Research about vertical load transfer in CSEs has flourished globally in the past few decades, advancing both fundamental understanding and related design procedures for practice (DGGT 2012; Sloan et al. 2014; BSI 2016; van Eekelen and Brugman 2016; Schaefer et al. 2017).

In the Schaefer et al. (2017) CSE design recommendations for US practice, and with reference to the British standards (BSI 2010), consideration is given to vertical load transfer and settlement, as well as lateral spreading. Herein, lateral spreading is defined as the lateral displacements induced by lateral earth pressures in the embankment and foundation. If excessive, lateral spreading can lead to failure of the embankment, the piled foundation, or the geosynthetic reinforcement in the LTP. Schaefer et al. (2017) gives consideration to lateral spreading in CSEs via the ultimate limit state design for lateral sliding. Assumptions are made for the failure mechanism and the driving and resisting thrusts, including the geosynthetic tensile resistance. In this paper, the current procedure for lateral spreading analysis is first discussed. This is followed by comparisons of the lateral thrust distribution assumed in design with results from 140 CSE scenarios as obtained from a three-dimensional (3D) numerical parametric study. The results and discussions of lateral thrust distribution as presented in this paper are intended to improve fundamental understanding of lateral spreading mechanics in CSEs and thereby move toward improving future design recommendations.

Design for Lateral Spreading

BSI (2016) and Schaefer et al. (2017) recommend the analysis of lateral spreading in CSEs via the ultimate limit state of lateral sliding, in which failure is assumed to occur by sliding of the embankment fill over the foundation surface in response to active lateral earth pressures in the embankment. The driving lateral thrust, P_{Lat}, is calculated using Eq. (1), where K_a is the active lateral earth pressure coefficient, γ is the unit weight of the embankment soil, H_{emb} is the embankment height, and q is the surcharge pressure:

$$P_{Lat} = K_a \left[\gamma \left(\frac{H_{emb}^2}{2} \right) + q H_{emb} \right] \quad (1)$$

A resisting lateral force, R_{ls}, is provided by the undrained shear strength (s_u) of the foundation soil mobilized over the length beneath the embankment slope (L_s), as follows:

[1]Graduate Student Researcher, Charles E. Via Jr. Dept. of Civil and Environmental Engineering, Virginia Tech, Blacksburg, VA 24060 (corresponding author). ORCID: https://orcid.org/0000-0002-3223-5272. Email: zhanyuh8@vt.edu

[2]Assistant Professor, Dept. of Civil and Environmental Engineering, Univ. of California, Davis, CA 95616. ORCID: https://orcid.org/0000-0001-5494-497X

[3]Professor, Charles E. Via Jr. Dept. of Civil and Environmental Engineering, Virginia Tech, Blacksburg, VA 24060.

© ASCE   04020126-1   J. Geotech. Geoenviron. Eng.

J. Geotech. Geoenviron. Eng., 2020, 146(11): 04020126

$$R_{ls} = L_s s_u \qquad (2)$$

If a factor of safety of 1.5 is not achieved for the ratio of R_{ls} to P_{Lat}, then geosynthetic reinforcement is recommended using one of two methods (Schaefer et al. 2017): (1) using a single layer, the design tensile load is calculated as the sum of the demand from vertical load transfer and lateral sliding (P_{Lat}); or (2) using two layers, one biaxial layer carries the design tensile load from vertical load transfer, and a second uniaxial layer carries P_{Lat}. Method 2 is recommended by Schaefer et al. (2017) because both the properties of the geosynthetic and the tensile demand are direction-dependent. The ultimate tensile strength of the geosynthetic is reduced by a safety factor of 1.5, as well as by factors accounting for durability, installation damage, and creep, to result in an allowable tensile strength that must equal or exceed the design tensile load.

Study Motivations

The analysis of lateral spreading via the ultimate limit state of lateral sliding assumes failure is only in the embankment, and it thus neglects lateral earth pressures in the foundation. However, only part of the embankment and service loading is carried by the columns, and the portion of vertical load carried by the subsoil between columns induces increased lateral earth pressures in the foundation soil. The lateral earth pressures in both the embankment and the foundation change with consolidation and development of soil arching. Thus, whether the embankment thrust should be calculated assuming an active condition and how the geosynthetic responds in tension under the influence of a changing total lateral thrust (i.e., from incremental earth pressures in both the embankment and foundation soils) are uncertainties in CSE design.

Despite limitations in the design assumptions for CSE lateral spreading analysis, limited research has been conducted to examine the CSE lateral thrust distribution. Farag (2008) measured the horizontal earth pressures in the embankment of a small-scale experimental CSE, but the resulting thrust was lower than the theoretical Rankine active thrust. Chen et al. (2016) examined the geosynthetic tension in a full-scale experimental CSE at the end of construction and before subsoil consolidation, in which the undrained subsoil was modeled using water bags. They found the tension to be highest at the centerline and near zero at the shoulder and concluded that the results were affected by inadequate development length in the reinforcement. Research using numerical techniques has focused on the CSE vertical load distribution between columns and subsoil, but not on the lateral thrust distribution in the embankment, foundation, and geosynthetic reinforcement (Ariyarathne et al. 2013a, b; Bhasi and Rajagopal 2013, 2014, 2015; Borges and Marques 2011; Han and Gabr 2002; Huang and Han 2009, 2010; Jamsawang et al. 2016; Jenck et al. 2009; Liu et al. 2007; Liu and Rowe 2016; Mahdavi et al. 2016; Nunez et al. 2013; Rowe and Liu 2015; Stewart et al. 2004; Yapage and Liyanapathirana 2014; Yapage et al. 2014; Ye et al. 2016; Yu et al. 2016; Zheng et al. 2009; Zhuang and Wang 2016). In this study, a numerical parametric study was used to analyze the lateral thrust distribution of CSEs for a wide range of conditions.

Definitions of Lateral Thrust

The lateral thrusts as discussed in this study differ from the active embankment lateral thrust, P_{Lat}, from Eq. (1). Any discussion of thrust henceforth refers to the following definitions:

Embankment thrust: the integration of the total lateral stress along a vertical plane from the foundation surface to the embankment surface (locations are annotated in Fig. 1).

Foundation thrust: the integration of the increment of lateral stress produced in the foundation (due to the increment of vertical
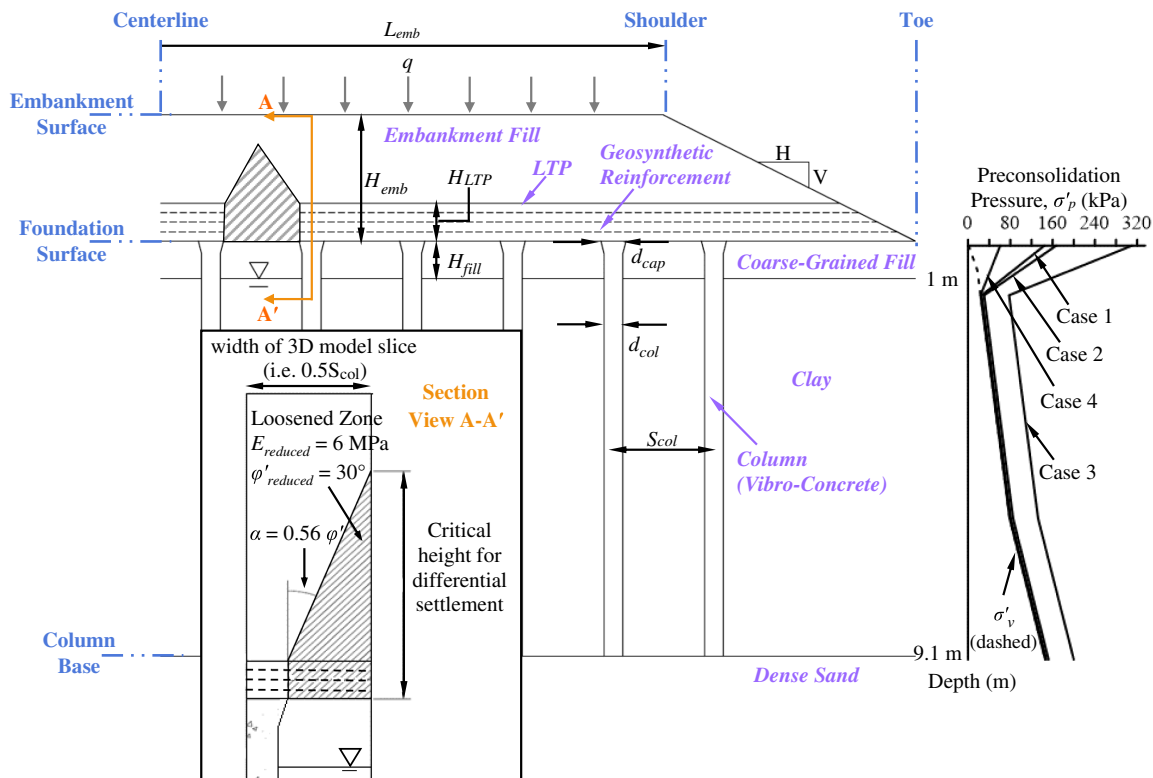

Fig. 1. CSE schematic including geometry of loosened zones in embankment.

© ASCE   04020126-2   J. Geotech. Geoenviron. Eng.

J. Geotech. Geoenviron. Eng., 2020, 146(11): 04020126

loading in the subsoil between columns) along a vertical plane from the column base elevation to the foundation surface.

Lateral thrust: the sum of the embankment and foundation thrusts, if the vertical plane examined is at the centerline or the shoulder, or only the foundation thrust, if the vertical plane is at the toe.

Geosynthetic tension: the tension in the transverse direction at the location of interest (i.e., at the centerline or shoulder locations).

Parametric Study Using Undrained-Dissipated Analyses

Complexities associated with the CSE lateral thrust distribution require a computation method that can account for the effects of time on soil arching and foundation pore water pressures. However, the analysis of deformation and pore water pressure histories could be computationally expensive, depending on the size of the numerical domain and the material properties. Huang et al. (2018) established that lateral spreading in CSEs can be instead analyzed using limiting cases, based on case history records of vertical earth pressure distributions and geosynthetic strains. The limiting case of undrained end-of-construction calculates the largest increment of earth pressure in the foundation. This is the result of limiting subsoil settlement and development of soil arching in the embankment under full embankment loading. The other limiting case of long-term dissipated excess pore pressures produces the largest geosynthetic strain and tension, as a result of increasing geosynthetic vertical deflection with subsoil consolidation. Both the foundation earth pressures, which contribute to the foundation thrust, and geosynthetic tension are quantities of interest in the analysis of CSE lateral thrust distribution.

The two limiting cases can be represented numerically using the undrained-dissipated approach (Huang et al. 2018), which computes an undrained end-of-construction state and a long-term dissipated state in succession. The method for computing consolidation was validated in one of the authors' previous works (Huang et al. 2018) and is summarized here. First, undrained loading occurs by excess pore pressure development in the clay during embankment construction through the application of an effective stress model (i.e., Modified Cam Clay). An undrained end-of-construction state is computed after application of full embankment loading. Next, all excess pore water pressures are dissipated by manually returning pore pressures to the hydrostatic condition. In this long-term dissipated state, consolidation deformations are computed given the changes in effective stress. The manual dissipation method and the resulting consolidation deformations were validated using benchmark solutions for a one-dimensional (1D) consolidation example and consolidation under a strip load of limited lateral extent.

Following validation, the undrained-dissipated approach was applied for the calibration and analyses of a 3D half-embankment slice model (Huang et al. 2019) using field instrumented data from an embankment case history reported in Liu et al. (2007). Calibrated material parameters that represent the loosening of select embankment zones during development of soil arching are also applied to the long-term dissipated analyses in the current study. One such loosened zone is shaded in Fig. 1. These domed regions in the embankment above the subsoil have been observed in field-scale embankments and bench-scale tests to experience shear, decrease in normal stress and density with the redistribution of vertical loading (McGuire 2011; Sloan 2011). The geometry of the loosened zone, in terms of an angle inclined from the vertical (α), can be determined using a correlation to the fill's effective friction angle

(φ') (McGuire 2011). The properties of the loosened zones can be represented using reduced values of Young's modulus (E_{reduced}) and reduced values of friction angle ($\varphi'_{\text{reduced}}$). Using $E_{\text{reduced}} = 6$ MPa and $\varphi'_{\text{reduced}} = 30°$ as the calibrated properties of the loosened zones, calculations of settlements and vertical load distribution at the subgrade level reached good agreement with long-term field recordings. These same calibrated values were adopted in the dissipated analysis of all CSE scenarios in the current parametric study.

Scope of Study

A parametric study totaling 140 scenarios was performed using a half-embankment domain in FLAC3D 5.01. An undrained end-of-construction and a long-term dissipated state was computed for each CSE scenario using the undrained-dissipated approach (Huang et al. 2018). Numerical parametric studies have been used to examine CSE system response under change of individual parameters (Bhasi and Rajagopal 2014; Borges and Marques 2011; Chai et al. 2017; Farag 2008; Huang and Han 2010; Jennings and Naughton 2011; Liu and Rowe 2016; Mahdavi et al. 2016; Shrestha et al. 2015; Yapage and Liyanapathirana 2014; Zhuang and Wang 2015, 2016). In this investigation, parameters were varied individually and in combinations, as discussed subsequently.

This study used variations in 14 parameters that are integral to CSE design. The range of parameter values are listed in Table 1, and values of design parameters were obtained from an experienced CSE designer (J. G. Collin, personal communication, 2018). Some of the examined variables are illustrated in the CSE schematic in Fig. 1.

It was impossible to investigate all scenarios using the range of parameter values, and thus 10 base cases encompassing a wide range of conditions were selected (Table 2). Parameters were typically varied one at a time from base case conditions. Some scenarios varied from the base case by two or three parameters to examine different combinations of geosynthetic design at different embankment heights. Base case BC1 was recommended by Collin (J. G. Collin, personal communication, 2018); BC2 to BC5 were developed to investigate the CSE response for different conditions of subgrade support and column area replacement ratio (ARR) within the typical range of 2.5%–10%; BC6 was designed to investigate edge instability in a tall embankment (i.e., instability downstream of outermost column); BC7 and BC8 were marginal cases for investigating global instability, using very low column ARRs; and BC9 and BC10 used a ratio of R_{ls} to P_{Lat} less than 1.5. Although geosynthetic reinforcement was required in only BC9, BC10, and corresponding variations for the purpose of mitigating lateral spreading (Schaefer et al. 2017), it was included in the majority of the 140 scenarios such that its response could be investigated for a wide range of conditions. Interested readers are directed to the supplemental materials file for a complete list of investigated scenarios.

Some aspects of the model were kept constant as parameters were varied. Above the bearing layer, the foundation thickness was kept constant at 9.1 m (30 ft), such that the clay thickness varied between 6.4 m (21 ft) and 9.1 m (30 ft) depending on variations in the foundation fill thickness (H_{fill}). This range of clay thickness has been reported in several CSE case histories (Almeida et al. 2007; Bell et al. 1994; Holmberg 1978; Lai et al. 2006; Reid and Buchanan 1984) and was selected to avoid excessive computation time associated with a larger numerical domain. The groundwater table remained at a depth of 0.91 m (3 ft) from the foundation surface. The columns had properties corresponding to unreinforced

© ASCE   04020126-3   J. Geotech. Geoenviron. Eng.

J. Geotech. Geoenviron. Eng., 2020, 146(11): 04020126

Table 1. Parameters and range of values investigated

Parameter	Parameter values
Embankment height (H_{emb})	1.5, 3.0, 4.6, and 6.1 m (5, 10, 15, and 20 ft)
LTP thickness (H_{LTP})	0.61, 0.91, and 1.2 m (2, 3, and 4 ft)
Foundation fill thickness (H_{fill})	0, 0.91, 1.8, and 2.7 m (0, 3, 6, and 9 ft)
Center-to-center column spacing (S_{col})	1.8, 2.4, and 3.0 m (6.0, 8.0, and 10.0 ft)
Cap diameter (d_{cap})	0.61 and 0.91 m (24 and 36 in.)
Column diameter (d_{col})	0.36, 0.46, and 0.61 m (14, 18, and 24 in.)
Embankment slope	3H:2V, 2H:1V
Shoulder-to-shoulder embankment width (L_{emb})	10, 24, and 40 m (± 2 m) (32, 80, and 128 ft)
Column group lateral extent (N_{col})	-1, 0, $+1$, $+2$ number of columns relative to column lateral group extent required for preventing edge instability (BSI 2016)
Number of geosynthetic layers (N_{geo})	0, 1, 2, 3
Geosynthetic stiffness (J)	300, 2,000, and 8,000 kN/m (20,500, 137,000, and 548,000 lb/ft)
Embankment fill friction angle (φ'_{emb})	34°, 40°, and 50°
	Young's modulus, Poisson's ratio, and unit weight (values in Table 3)
Foundation preconsolidation pressure (σ'_p)	Cases 1–4 (Fig. 1)
Service loading (q)	0 and 14 kPa (0 and 300 psf)

Note: Dependent variables are italicized.

Table 2. Base cases and corresponding parameter values

Base case	H_{emb} (m)	H_{LTP} (m)	H_{fill} (m)	S_{col} (m)	d_{cap} (m)	d_{col} (m)	Slope (H:V)	L_{emb} (m)	N_{col}	N_{geo}	J (kN/m)	φ'_{emb} (degrees)	σ'_p	q (kPa)
BC1	3.0	0.91	0.91	2.4	0.61	0.46	2:1	24	0	3	300	40	Case 2	0
BC2	3.0	0.91	2.7	1.8	0.61	0.61	2:1	24	0	0	—	40	Case 2	0
BC3	3.0	0.91	0	1.8	0.61	0.61	2:1	24	0	0	—	40	Case 1	0
BC4	4.6	0.91	2.7	3.0	0.61	0.61	2:1	24	0	0	—	40	Case 2	0
BC5	4.6	0.91	0	3.0	0.61	0.61	2:1	24	0	0	—	40	Case 1	0
BC6	6.1	0.91	0.91	1.8	0.61	0.61	2:1	22	0	2	8,000	40	Case 2	0
BC7	4.6	0.91	0	3.0	0.36	0.36	3:2	25	0	0	—	40	Case 1	0
BC8	6.1	0.91	0	3.0	0.61	0.46	3:2	25	0	0	—	40	Case 1	0
BC9	3.0	0.91	0	1.8	0.61	0.46	3:2	25	0	1	300	40	Case 4	14
BC10	4.6	0.91	0	3.0	0.61	0.61	3:2	25	0	1	2,000	40	Case 4	14

concrete and a constant length of 9.1 m that extended to the bearing layer.

Results are presented in terms of the lateral thrust distribution:
1. Comparison of lateral thrust in undrained end-of-construction condition versus long-term dissipated condition;
2. Comparison of lateral thrust at different locations of embankment in transverse direction (i.e., centerline, shoulder, and toe, as annotated in Fig. 1);
3. Comparison of thrust in embankment versus thrust in foundation;
4. Portion of lateral thrust resisted in foundation at embankment toe, by tension in geosynthetic reinforcement, and by shear at column base elevation (Fig. 1);
5. Comparison of computed embankment lateral thrust to theoretical active embankment thrust used in design [i.e., P_{Lat} from Eq. (1)]; and
6. Comparison of computed geosynthetic tension to design tensile load (i.e., P_{Lat}) for cases where geosynthetic reinforcement is required in design to mitigate lateral spreading.

The analysis of thrust at different embankment locations and pore water pressure conditions represents an extension, as well as a point of comparison, to the analysis of driving thrust based on an active condition in the embankment, as in Schaefer et al. (2017). Select preliminary results from the parametric study are presented in Huang et al. (2020). This paper presents the complete analysis of lateral thrust distribution in CSEs as synthesized from the same study. New results are provided for lateral thrust at the shoulder location (i.e., expansion on Item 2), the comparison of thrust in the embankment versus thrust in the foundation (i.e., Item 3), the portion of lateral thrust resisted by tension in the geosynthetic reinforcement (i.e., expansion on Item 4), the

comparison of computed embankment lateral thrust to P_{Lat} (i.e., Item 5), and the comparison of geosynthetic tension to P_{Lat} (i.e., Item 6).

Numerical Procedure

Validated numerical modeling procedures were selected (Huang et al. 2018) and applied to the analyses of a field CSE case history with calibration of material parameters (Huang et al. 2019). Many aspects of the numerical model are inherited from the studies cited and are summarized as follows.

Constitutive models and material properties are listed in Table 3 for the soils and columns and in Table 4 for the geosynthetic reinforcement. The choice of constitutive models was made in consideration of ease of adoption and computational efficiency. The latter is important for computing a large number of CSE scenarios. All soils, except for the clay, were modeled as linearly elastic and perfectly plastic with the Mohr-Coulomb failure criterion. The clay was modeled with the Modified Cam Clay model. The columns were also modeled as linearly elastic and perfectly plastic with the Mohr-Coulomb failure criterion, but including a tensile strength (σ_t) (ACI 2011; Huang 2019; Pul et al. 2017; Schädlich and Schweiger 2014). Huang et al. (2019) reported large bending moments and tension due to flexure in linear elastic CSE columns, and thus a failure criterion with a limit on the tensile strength was adopted for the columns in this study. The geosynthetic reinforcement was modeled using orthotropic linear elastic structural geogrid elements of the constant strain triangle type (Itasca 2013), which can sustain membrane stress but not bending. The orthotropic model is representative of biaxial geogrids, which

© ASCE 04020126-4 J. Geotech. Geoenviron. Eng.

J. Geotech. Geoenviron. Eng., 2020, 146(11): 04020126

Table 3. Material properties of soils and columns

Material	γ (kN/m³)	Model	φ' (degrees)	c' (kPa)	σ_t (kPa)	E (MPa)	ν	λ	κ	M	e_1
Embankment fill											
Loose sand	17.3	MC	35	0	—	17	0.30	—	—	—	—
Dense sand	18.9	MC	40	0	—	36	0.26	—	—	—	—
Gravel	22.0	MC	50	0	—	120	0.20	—	—	—	—
LTP (gravel)	22.0	MC	50	0	—	120	0.20	—	—	—	—
Foundation fill	18.1	MC	37	0	—	24	0.28	—	—	—	—
Clay	16.5	MCC	—	—	—	—	0.37	0.17	0.017	0.98	2.75
Bearing sand	22.8	MC	45	0	—	43	0.23	—	—	—	—
Concrete column	23.6	MC	43	3,700	1,580	21,500	0.20	—	—	—	—

Note: MC = Mohr-Coulomb; MCC = modified cam clay; three different materials were investigated for the embankment fill and foundation fill; e_1 is the void ratio at a reference pressure of 0.048 kPa (1 psf); and $E = 6$ MPa and $\varphi' = 30°$ were applied to select embankment zones in dissipated analyses to represent loosening of fill due to vertical load distribution.

Table 4. Material properties of geosynthetic reinforcement

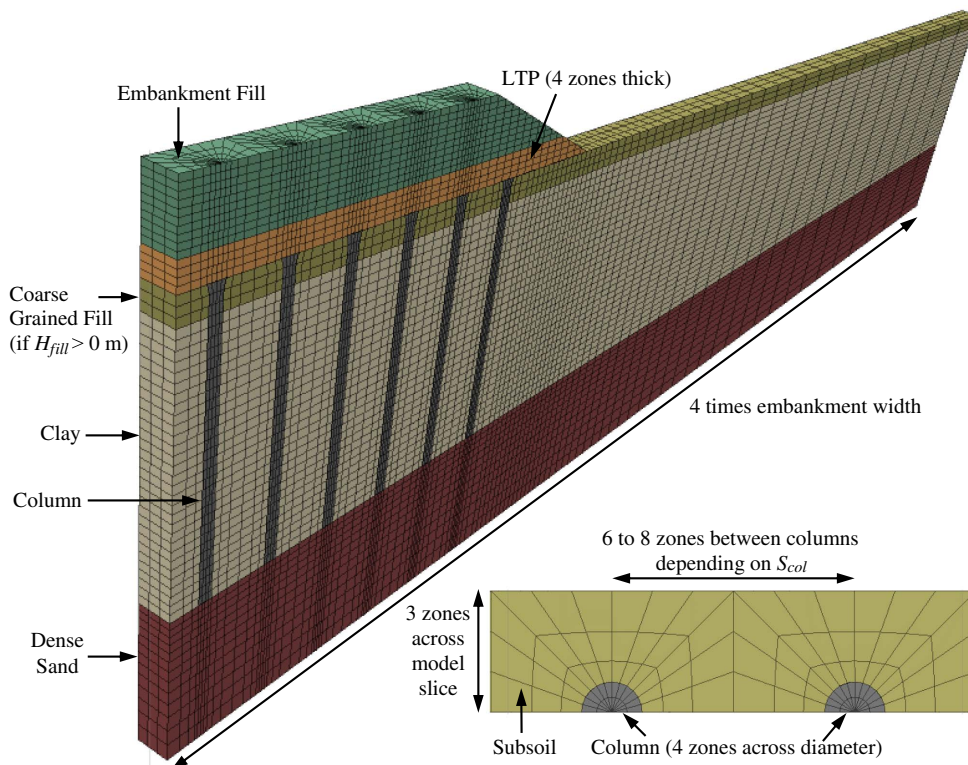| Model	J (kN/m)	ν	G (kPa)
Orthotropic linear elastic	300, 2,000, and 8,000	0	1

Note: $\nu = 0$ in both longitudinal and transverse directions.

have stiffness mainly in orthogonal directions. The geosynthetic reinforcement and columns can interact with surrounding zones through interfaces, whose properties are described in detail in the supplemental materials file.

The embankment model geometry, discretization, and boundary conditions were selected to appropriately represent the physical domain of the problem while ensuring computational efficiency. The model consisted of a 3D half-embankment slice with zone discretization as illustrated in Fig. 2. The half-embankment geometry is appropriate for the analysis of lateral thrust distribution in symmetric embankments. The discretization consisted of a minimum of 34,000 grid points (locations of displacement calculation), and the lateral extent was 4 times the embankment width and at least 13 times the embankment height. These quantities were determined from convergence studies conducted separately. Boundary conditions consisted of a free surface at the top, a pinned surface at the model base, and rollers on all other external surfaces.

Analyses were conducted using the large-strain mode in FLAC3D 5.01 and the following loading sequence. In situ foundation stresses were assigned and mechanical equilibrium was established. Columns had the same density as the surrounding soils, and zones in the LTP and embankment fill were assigned null material properties. Column installation was then modeled by gradually increasing the column density while solving for equilibrium. Next, undrained loading and consolidation were modeled using the undrained-dissipated approach (described in the section "Parametric

Fig. 2. Model discretization.

© ASCE   04020126-5   J. Geotech. Geoenviron. Eng.

J. Geotech. Geoenviron. Eng., 2020, 146(11): 04020126

Study using Undrained-Dissipated Analyses"). During undrained embankment construction, drainage was disabled in the submerged foundation clay and excess pore water pressures as induced by embankment loading were computed. The LTP and embankment were constructed in lifts, where zones were changed from null to Mohr-Coulomb materials, and their density was gradually increased while solving for equilibrium. The construction of the final lift marked the undrained end-of-construction state. The subsequent dissipated analysis consisted of applying $E_{reduced} = 6$ MPa and $\varphi'_{reduced} = 30°$ in select embankment zones to represent the loosening of fill during development of soil arching (Fig. 1, section view A-A′). Excess pore water pressures were dissipated in one step. Consolidation deformations and mechanical equilibrium were solved for the long-term dissipated state.

Data Processing: Extraction of Thrusts

Computations provided lateral earth pressures and geogrid tensions in discretized zones, and these quantities were further processed to obtain thrusts. The embankment thrust was calculated by integrating the average total lateral stress at each zone elevation along a vertical plane from the foundation surface to the embankment surface. The foundation thrust was calculated in a similar manner, but by integrating the average incremental lateral stress from the column base elevation to the foundation surface. The foundation and embankment thrusts were summed to obtain the total lateral thrust along a vertical plane. The geosynthetic tension was calculated by averaging the tensile force in geogrid elements closest to the vertical plane of interest. Note that the vertical planes at the centerline and shoulder were mid-distance between columns, so the
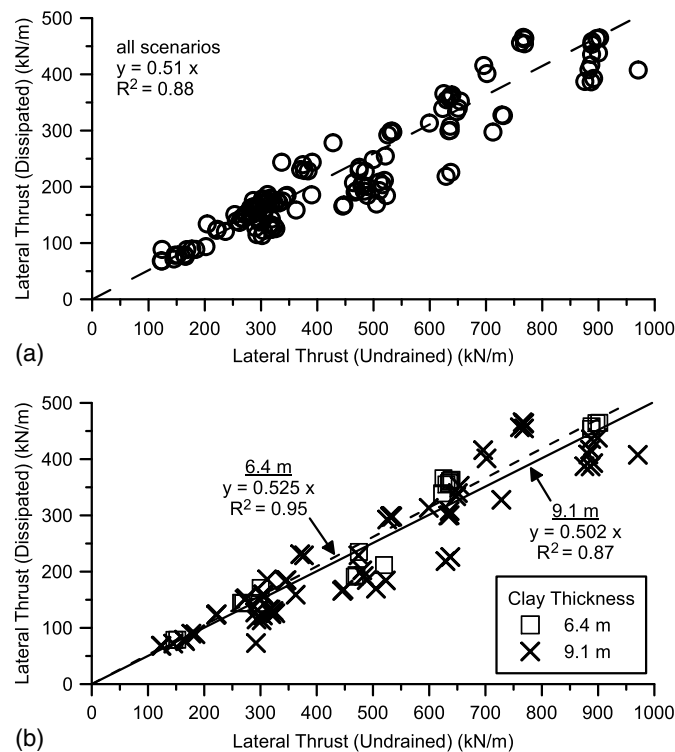
geosynthetic tension at these locations had no vertical component and were minimally influenced by column edge effects.

Results and Discussion

Computed results are provided for the lateral thrust distribution in the embankment, geosynthetic, and foundation along vertical planes at the embankment centerline, shoulder, and toe (locations annotated in Fig. 1) for the two limiting cases (undrained end-of-construction and long-term dissipated).

Comparison of Thrust in Transverse Direction (Centerline, Shoulder, and Toe)

As shown in Figs. 3(a and b), the lateral thrust at the centerline in the dissipated condition is approximately half that in the undrained condition, and this correlation is not significantly affected by the clay thickness for the range examined. Excess pore water pressure dissipation directly reduces the total lateral thrust, and clay consolidation transfers vertical loads from the clay to the columns and thereby also reduces the lateral thrust.

The thrusts at the shoulder and toe locations also decrease with excess pore pressure dissipation, and relative to the centerline thrust, they are smaller in magnitude, with a few exceptions [Figs. 4(a and b)]. The decrease in thrust with distance from the centerline was found in all scenarios in the undrained condition
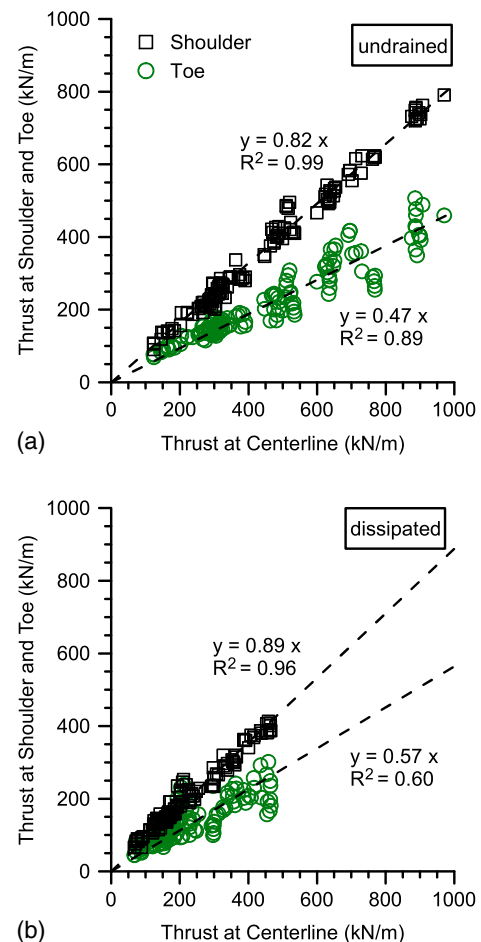
Fig. 3. Lateral thrust at centerline in dissipated versus undrained conditions for (a) all scenarios; and (b) scenarios with clay thicknesses of 6.4 and 9.1 m.

Fig. 4. Lateral thrust at shoulder and toe locations versus lateral thrust at centerline for (a) undrained end-of-construction; and (b) dissipated long-term.

© ASCE 04020126-6 J. Geotech. Geoenviron. Eng.

J. Geotech. Geoenviron. Eng., 2020, 146(11): 04020126

[Fig. 4(a)], with thrusts at the shoulder and toe locations being 82% and 47% of the centerline thrust, respectively. More variation was found for the dissipated condition. Although thrusts at the shoulder and toe locations are respectively 89% and 57% of the centerline thrust [Fig. 4(b)], 25 scenarios calculated the largest thrust at the shoulder, and one scenario calculated the largest thrust at the toe. These scenarios have in common a wide distance from the outer edge of the outermost column to the embankment toe or large settlement at the shoulder relative to that at the centerline.

The trends in the relative magnitudes of thrust at the centerline, shoulder, and toe locations have several implications. In terms of movement, the general trend of decreasing lateral thrust with increasing distance from the centerline in the undrained condition is consistent with reduced lateral restraint at the edge and movement of the embankment away from the centerline. The magnitude of thrusts at the toe is smaller than at the shoulder and centerline. However, the thrusts at the toe still represent a significant portion of the resistance to the driving thrust in both the undrained and dissipated conditions, and more so in the dissipated condition. The scatter in correlation between the thrusts at the toe and centerline is significantly reduced when the data are grouped according to foundation preconsolidation pressure (σ'_p) and geosynthetic stiffness (J). As illustrated in Figs. 5(a–d) for the preconsolidation pressure distribution shown in Case 1 of Fig. 1, the thrust at the toe relative to the thrust at the centerline decreased with increasing J, indicating a redistribution of resisting thrust to the stiffer geosynthetics. However, the resisting foundation thrust at the toe remained significant for all geosynthetic conditions.

Thrust Distribution in Embankment and Foundation

Figs. 6(a–d) illustrate the embankment thrust versus the foundation thrust at the centerline and shoulder locations for the undrained and dissipated conditions. Owing to scatter in the data resulting from the wide range of parameter values investigated, results are discussed in terms of trends rather than correlations. In the undrained condition, the foundation thrust exceeds the embankment thrust at all locations across the embankment. The foundation thrusts are larger in the undrained condition because the foundation supports the greatest increment of loading when settlement and soil arching are limited. In the dissipated condition, the embankment thrust increases in magnitude and the foundation thrust decreases in magnitude compared to the undrained condition. The embankment thrust exceeds the foundation thrust in a number of scenarios, particularly for the smallest column spacing (S_{col}) of 1.8 m (6 ft). This trend is explained by the development of soil arching and subsoil consolidation in the long-term dissipated condition. The development of arching results in larger lateral stresses in the embankment, while the simultaneous increase in differential settlement at the subgrade level facilitates vertical load transfer to columns and decreases the increment of loading in the subsoil. The ratio of embankment thrust to foundation thrust is larger for smaller S_{col} due to greater effectiveness in vertical load transfer to columns. Figs. 6(c and d) also show that the embankment thrust is smaller at the shoulder than at the centerline in the dissipated condition, likely due to effects of the embankment slope on arching.

The question of whether the embankment thrust can be appropriately represented by the design active thrust (Schaefer et al. 2017) was investigated by comparing P_{Lat} [Eq. (1)] to the range of calculated embankment thrusts. Results are presented for scenarios with embankment heights of 3.0 m (10 ft), 4.6 m (15 ft), and 6.1 m (20 ft) and for the centerline and shoulder locations [Figs. 7(a and b), respectively]. In all cases, the calculated embankment thrust is larger than P_{Lat}, though the undrained cases are closer, and marginal cases with developing global instability in the undrained condition are the closest. The calculated
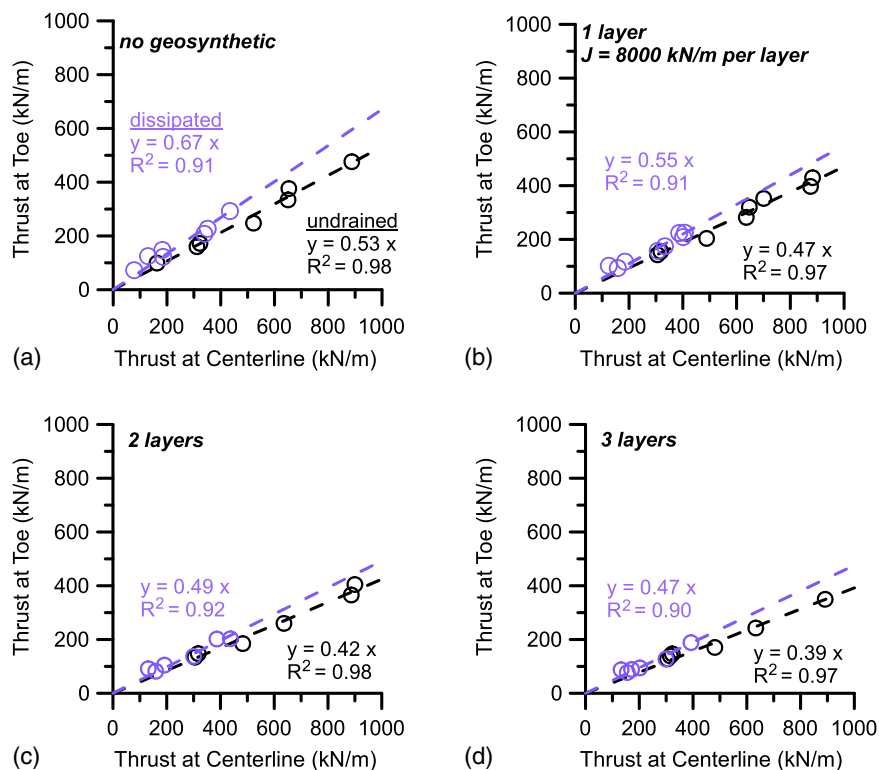

Fig. 5. Thrust at toe versus thrust at centerline in undrained and dissipated conditions for scenarios with Case 1 preconsolidation pressure using different number of geosynthetic layers ($J = 8,000$ kN/m per layer).
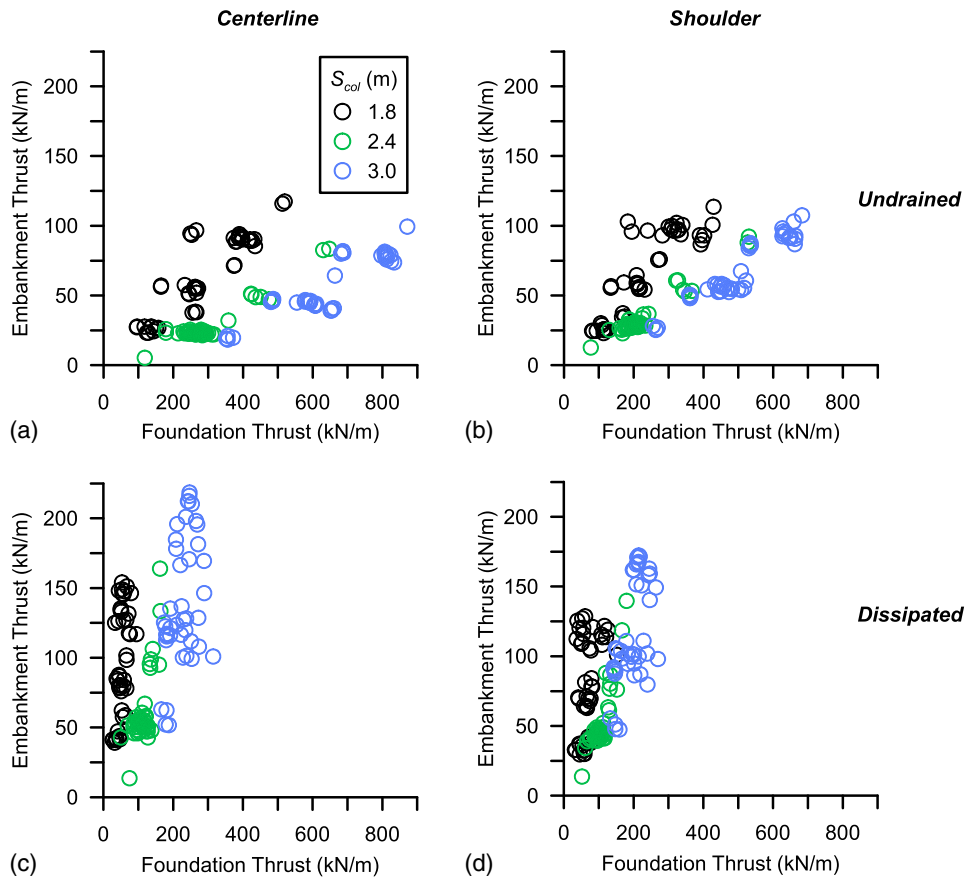
© ASCE   04020126-7   J. Geotech. Geoenviron. Eng.

J. Geotech. Geoenviron. Eng., 2020, 146(11): 04020126

Fig. 6. Embankment thrust versus foundation thrust at different locations and limiting conditions.
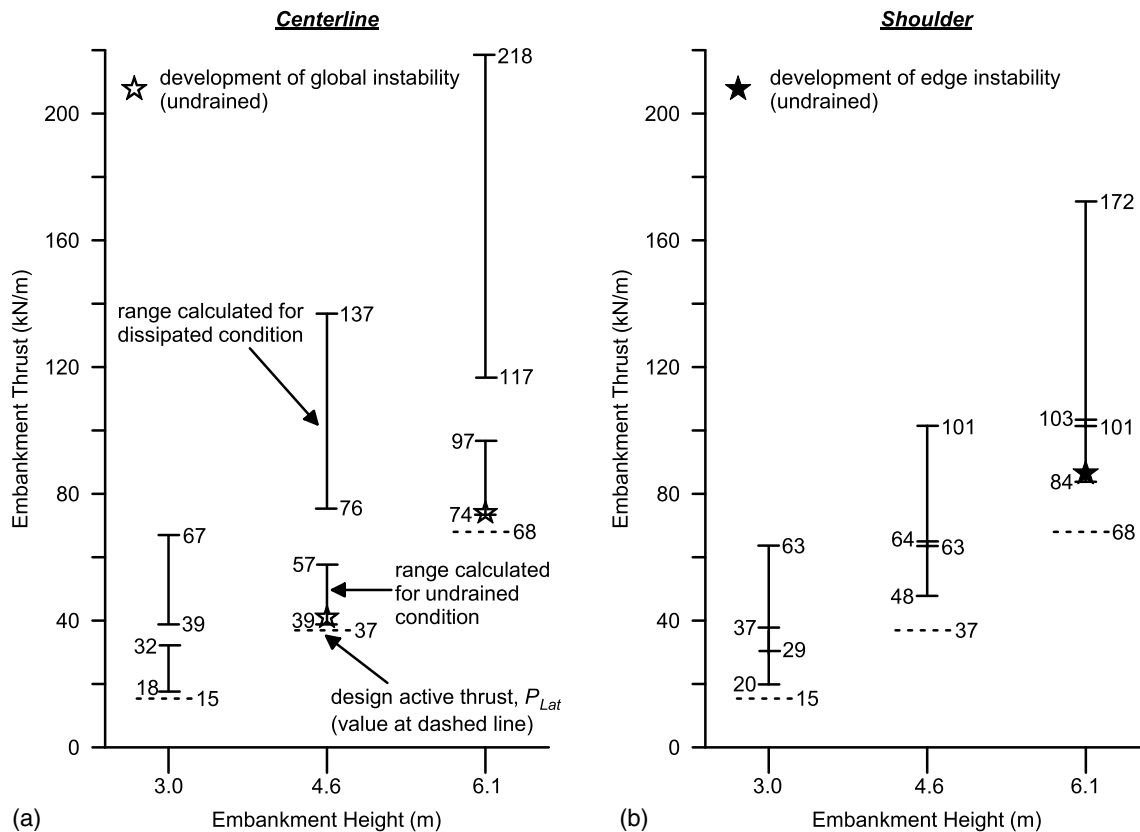
Fig. 7. Comparison of calculated embankment lateral thrust versus design active thrust for different embankment heights.

embankment thrusts exceed P_{Lat} because full active conditions are generally not developed in the embankment. Embankment thrusts are larger in the dissipated condition due to the development of soil arching and increase in lateral stresses in the embankment, corresponding to trends in Figs. 6(a–d).

Geosynthetic Tension

Geosynthetic tension is examined at the embankment centerline and shoulder locations for different column ARRs and geosynthetic stiffness (J) [Figs. 8(a–f)]. Results are exclusive to embankments with a height above the critical height, thereby satisfying the serviceability limit for differential settlement. Each data set includes many parameter variations besides geosynthetic stiffness and column ARR, which produces scatter. Nevertheless, the trends and upper limits of the geosynthetic contribution to resisting lateral thrust can be compared.

For all cases of J and column ARR, the geosynthetic tension is higher in the dissipated condition (orange versus blue data points),

and the upper limit in the ratio of geosynthetic tension to lateral thrust is approximately the same at the centerline and shoulder locations (dashed lines in plots on the left versus on the right). Geosynthetic tension is larger in the dissipated condition due to subsoil consolidation and increase in geosynthetic vertical deflection.

The upper limit in the ratio of geosynthetic tension to lateral thrust is more affected by J than location and column ARR. For typical column ARRs and $J = 300$ kN/m, the geosynthetic resists at most 2% and 7% of the thrust in the undrained and dissipated conditions, respectively. Most scenarios calculated geosynthetic tensions much lower than the upper limits, indicating that for cases of practical importance, the geosynthetics typically used in the US (J.G. Collin, personal communication, 2018) have limited utility in resisting lateral thrust. For typical column ARRs and $J = 8,000$ kN/m, the tensile resistance is increased respectively to 16% and 50%. The results in Figs. 8(a–f) and 5(a–d) all indicate that more lateral thrust is distributed in the geosynthetic and less thrust is distributed in the foundation at the toe when using geosynthetics of greater stiffness.
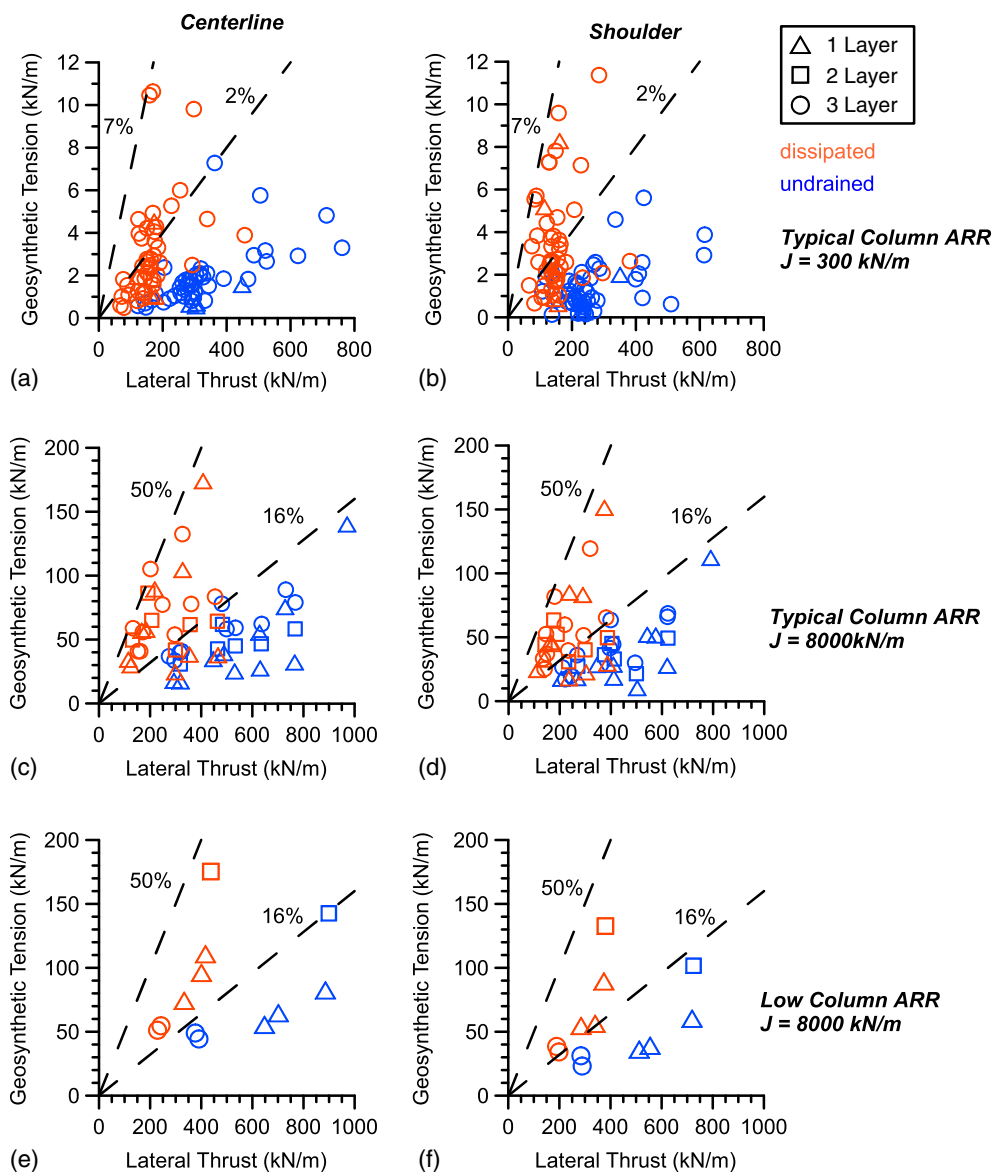

Fig. 8. Geosynthetic resistance of lateral thrust at centerline and shoulder locations for different column area replacement ratios and geosynthetic stiffnesses.

© ASCE 04020126-9 J. Geotech. Geoenviron. Eng.

J. Geotech. Geoenviron. Eng., 2020, 146(11): 04020126

Figs. 9(a–e) illustrate the geosynthetic tension at the shoulder location versus the geosynthetic design tensile load for lateral spreading design, which is assumed to equal the active lateral thrust in the embankment (i.e., P_{Lat}). Results are for scenarios in which geosynthetic reinforcement is required in design for mitigating lateral spreading (i.e., ratio of R_{ls} to P_{Lat} is less than 1.5). The figures show that the geosynthetic tension is not correlated to P_{Lat}. Instead, the tension developed depends on the geosynthetic stiffness (J) and how much the geosynthetic is being exercised, where it increases with increasing J, column spacing (S_{col}), and embankment height (H_{emb}). The resulting geosynthetic tension could be smaller or greater than P_{Lat}.

Lateral Force Equilibrium

Free body diagrams illustrating lateral force increments in the embankment, geosynthetic reinforcement, foundation, and shear force at the column base elevation are provided for three scenarios in Fig. 10. The scenarios represent different column ARR and geosynthetic designs, with properties provided in Table 5 and summarized here: (1) Scenario A is for a 3.0-m-tall embankment using typical column ARR and three layers of geosynthetics with $J = 300$ kN/m; (2) Scenario B is for a 6.1-m-tall embankment using typical column ARR and two layers of geosynthetics with $J = 8,000$ kN/m; and (3) Scenario C is for a 6.1-m-tall embankment using low column ARR and one layer of geosynthetic with $J = 8,000$ kN/m.

The following observations can be made for the lateral thrust distribution with reference to the free body diagrams in Fig. 10. The shear force at the column base elevation resists a significant portion of the driving thrust originating from the embankment and the foundation. During the dissipation of excess pore water

pressures, the total lateral thrust in the embankment and foundation at the centerline decreases, which is consistent with the trends shown in Fig. 4. Both the base shear and lateral thrust at the toe decrease in response to the decrease in centerline thrust. The effect is particularly marked for Scenario C, which has low column ARR and less subgrade support (i.e., soft clay extended to foundation surface). Fig. 10 shows that the geosynthetics in Scenario A provide a negligible contribution to lateral force equilibrium. The geosynthetics represented in Scenario A are typical of those used in US practice. The high-stiffness geosynthetics represented in Scenarios B and C make a larger contribution to satisfying lateral force equilibrium. Although the total geosynthetic stiffness for Scenario C is only half that of Scenario B, the geosynthetic reinforcement in Scenario C experiences larger tension in response to the larger lateral thrust at the centerline and shoulder.

Summary and Conclusions

Results from a 3D numerical parametric study totaling 140 scenarios for CSEs were synthesized and presented in terms of the lateral thrust distribution. Driving and resisting thrusts for lateral spreading analysis of CSEs were examined and quantified in relative proportions: (1) the embankment thrust calculated by integrating total lateral stresses over the embankment height; (2) the foundation thrust calculated by integrating incremental lateral stresses from the column base elevation to the foundation surface; (3) the geosynthetic tension; and (4) the shear force at the column base elevation (as required for analysis of lateral force equilibrium). Calculations were performed along vertical planes at the embankment centerline, shoulder, and toe and for the limiting cases of lateral spreading (i.e., undrained end-of-construction and long-term dissipated).
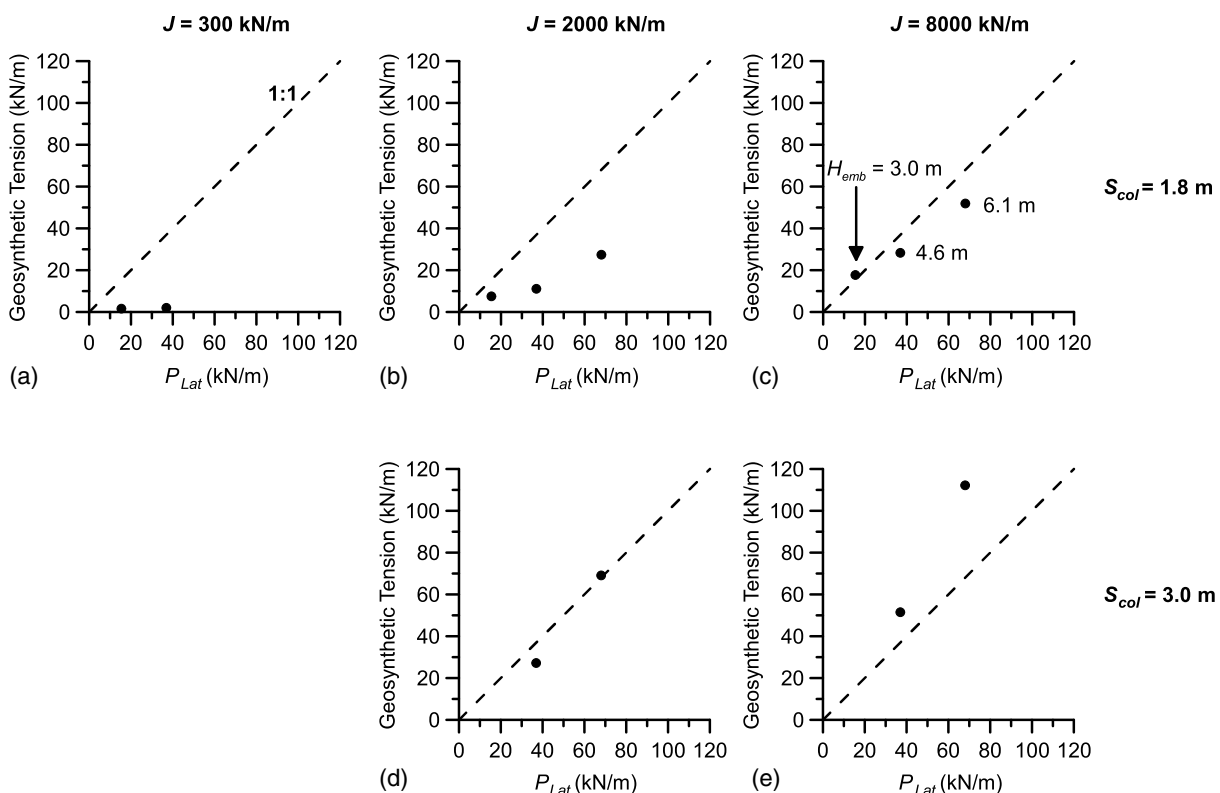

Fig. 9. Geosynthetic tension at shoulder versus P_{Lat} for scenarios requiring geosynthetic to mitigate lateral spreading (i.e., $R_{ls}/P_{Lat} < 1.5$).
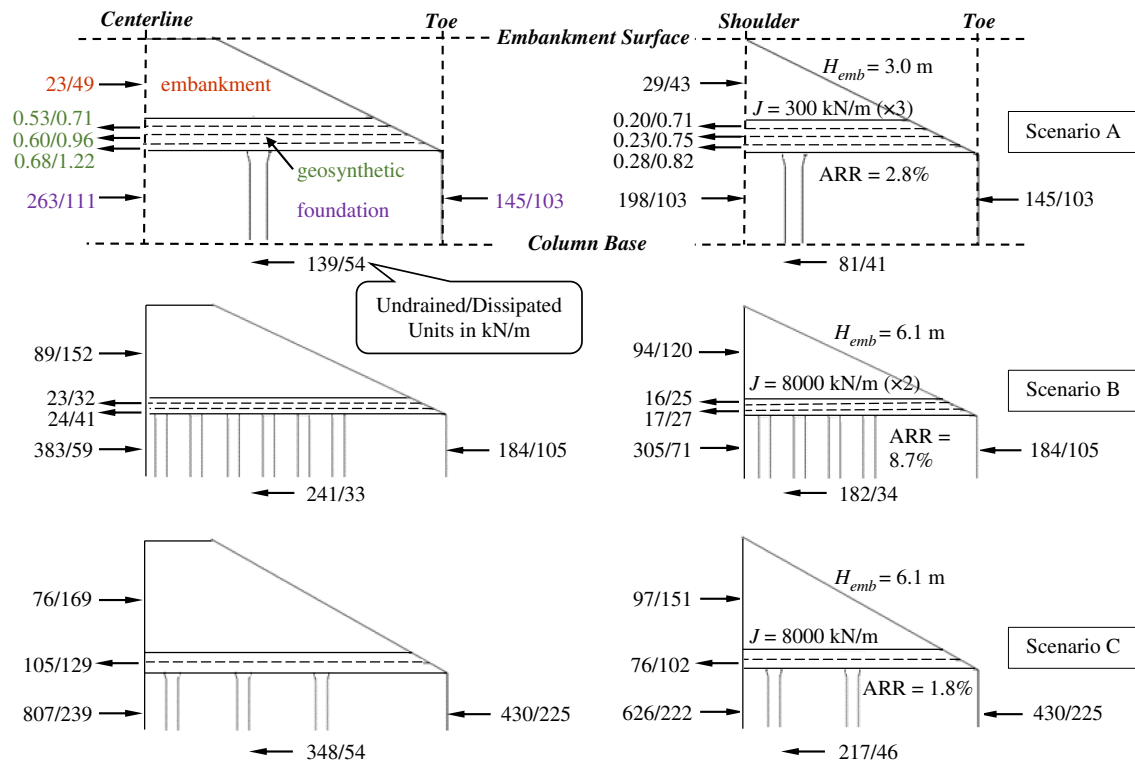
© ASCE 04020126-10 J. Geotech. Geoenviron. Eng.

J. Geotech. Geoenviron. Eng., 2020, 146(11): 04020126

Fig. 10. Free body diagrams of lateral thrust distribution (scenario geometries and material properties shown in Table 5); not to scale.

Table 5. Parameter values for scenarios adopted in investigation of lateral force equilibrium (Fig. 10)

H_{emb} (m)	H_{LTP} (m)	H_{fill} (m)	S_{col} (m)	d_{cap} (m)	d_{col} (m)	Slope(H:V)	L_{emb} (m)	N_{col}	N_{geo}	J (kN/m)	φ'_{emb} (degrees)	σ'_p	q (kPa)
			Scenario A (BC1)—typical column ARR and lightweight geosynthetic										
3.0	0.91	0.91	2.4	0.61	0.46	2:1	24	0	3	300	40	Case 2	0
			Scenario B—typical column ARR and heavyweight geosynthetic										
6.1	0.91	0.91	1.8	0.61	0.61	2:1	22	+2	2	8,000	40	Case 2	0
			Scenario C—low column ARR and heavyweight geosynthetic										
6.1	0.91	0	3.0	0.61	0.46	3:2	25	0	1	8,000	40	Case 1	0

Fundamental understanding of lateral spreading mechanics in CSEs was advanced through the analyses of lateral thrust distribution:

1. The driving thrust produced by the sum of embankment and foundation thrusts is resisted by the foundation thrust at the toe, geosynthetic tension, and base shear.
2. Pore water pressure conditions affect the relative magnitudes of thrust. The foundation thrust is largest in the undrained condition and decreases with excess pore water pressure dissipation. The embankment thrust is smallest in the undrained condition and increases with excess pore pressure dissipation and development of soil arching. The geosynthetic tension is smallest in the undrained condition and increases with excess pore pressure dissipation and vertical deflection. The base shear is largest in the undrained condition.
3. The foundation thrust contributes significantly to both the driving and resisting thrusts.
4. Geosynthetic tension increases with stiffness (J), and geosynthetics of greater stiffness resist a greater portion of the driving thrust.
5. No relationship exists between geosynthetic tension and active lateral thrust in the embankment (P_{Lat}) because the tension can be smaller or greater than P_{Lat} depending on the geosynthetic stiffness and how much the geosynthetic is being exercised.
6. The undrained condition is the most critical for lateral spreading:
   - Lateral thrust is largest at the centerline and decreases in magnitude toward the toe, consistent with a system tendency to spread laterally away from the centerline.
   - The embankment thrust is closest in value to the theoretical active thrust adopted for design, owing to the limited development of soil arching and vertical load transfer to columns. The smallest calculated embankment thrusts were found for cases with developing global instability in the undrained condition.
   - Both the geosynthetic tension and the portion of thrust resisted by the geosynthetic are smallest when vertical deflection is limited.
   - The base shear is largest in the undrained condition, indicating the greatest likelihood of approaching the shear strength prior to consolidation.
7. The CSE lateral thrust distribution for the critical undrained condition can be estimated using the following correlations:

© ASCE   04020126-11   J. Geotech. Geoenviron. Eng.

J. Geotech. Geoenviron. Eng., 2020, 146(11): 04020126

- The ratio of shoulder thrust to centerline thrust is approximately 80%.
- The ratio of thrust at the toe to centerline thrust is approximately 50%.
- The ratio of geosynthetic tension to centerline thrust depends on the geosynthetic stiffness (J). Using $J = 300$ kN/m, the ratio is at most 2%. Using $J = 8{,}000$ kN/m, the ratio is at most 16%. The maximum ratio of geosynthetic tension to thrust is approximately the same at the centerline and the shoulder.
- Remaining driving thrust is resisted by base shear.

Future work could expand upon the correlations by investigating conditions outside the scope of this study. CSEs integrated with mechanically stabilized earth wall systems could produce the worst slope condition for lateral spreading. The effect of column length could also be investigated. The current work could be extended to investigate potential failure mechanisms in CSEs and to establish whether they occur in the undrained condition, as suggested by results from the current study. Failure analyses should incorporate tensile failure in the geogrid elements, such that the geosynthetic influence on load path can be examined in addition to its contribution to resisting thrust.

Data Availability Statement

Some or all data, models, or code generated or used during the study are available from the corresponding by reasonable request.

Acknowledgments

Notation

The following symbols are used in this paper:

c' = effective cohesion;
d_{cap} = cap diameter;
d_{col} = column diameter;
E = Young's modulus;
E_{reduced} = reduced Young's modulus adopted in loosened embankment zones;
e_1 = void ratio at reference pressure;
G = shear modulus;
H_{emb} = embankment height;
H_{fill} = foundation fill thickness;
H_{LTP} = load transfer platform height (i.e., thickness);
J = geosynthetic stiffness;
K_a = coefficient of active lateral earth pressure;
L_{emb} = shoulder-to-shoulder embankment width;
L_s = length of foundation beneath embankment slope;
M = slope of critical state line;
N_{col} = number of columns in half-embankment model relative to column group extent required to prevent edge instability;
N_{geo} = number of geosynthetic layers;
P_{Lat} = active lateral thrust in embankment;
q = surcharge pressure loading;

R_{ls} = resisting thrust in foundation based on undrained shear strength;
S_{col} = center-to-center column spacing;
s_u = undrained shear strength;
α = angle of shear failure surface from vertical;
γ = unit weight;
κ = slope of recompression line;
λ = slope of virgin compression line;
ν = Poisson's ratio;
σ_t = tensile strength;
σ'_p = preconsolidation pressure;
σ'_v = effective vertical stress;
φ' = effective friction angle;
φ'_{emb} = effective friction angle of embankment fill;
φ'_{fill} = effective friction angle of foundation fill; and
$\varphi'_{\text{reduced}}$ = reduced effective friction angle adopted in loosened embankment zones.

Supplemental Materials

Table S1 is available online in the ASCE Library (www.ascelibrary.org).

References

ACI (American Concrete Institute). 2011. *Building code requirements for structural concrete and commentary.* ACI 318-11. Farmington Hills, MI: ACI.

Almeida, M. S. S., M. Ehrlich, A. P. Spotti, and M. E. S. Marques. 2007. "Embankment supported on piles with biaxial geogrids." *Proc. Inst. Civ. Eng. Geotech. Eng.* 160 (4): 185–192.

Ariyarathne, P., D. S. Liyanapathirana, and C. J. Leo. 2013a. "Comparison of different two-dimensional idealizations for a geosynthetic-reinforced pile-supported embankment." *Int. J. Geomech.* 13 (6): 754–768. https://doi.org/10.1061/(ASCE)GM.1943-5622.0000266.

Ariyarathne, P., D. S. Liyanapathirana, and C. J. Leo. 2013b. "Effect of geosynthetic creep on reinforced pile-supported embankment systems." *Geosynthetics Int.* 20 (6): 421–435. https://doi.org/10.1680/gein.13.00029.

Bell, A. L., C. Jenner, J. D. Maddison, and J. Vignoles. 1994. "Embankment support using geogrids with vibro concrete columns." In *Proc., 5th Int. Conf. on Geotextiles, Geomembranes and Related Products*, 335–338. Singapore: Southeast Asia Chapter of the International Geotextile Society.

Bhasi, A., and K. Rajagopal. 2013. "Numerical investigation of time dependent behavior of geosynthetic reinforced piled embankments." *Int. J. Geotech. Eng.* 7 (3): 232–240. https://doi.org/10.1179/1938636213Z.00000000031.

Bhasi, A., and K. Rajagopal. 2014. "Geosynthetic-reinforced piled embankments: Comparison of numerical and analytical methods." *Int. J. Geomech.* 15 (5): 04014074. https://doi.org/10.1061/(ASCE)GM.1943-5622.0000414.

Bhasi, A., and K. Rajagopal. 2015. "Numerical study of basal reinforced embankments supported on floating/end bearing piles considering pile–soil interaction." *Geotext. Geomembr.* 43 (6): 524–536. https://doi.org/10.1016/j.geotexmem.2015.05.003.

Borges, J. L., and D. O. Marques. 2011. "Geosynthetic-reinforced and jet grout column-supported embankments on soft soils: Numerical analysis and parametric study." *Comput. Geotech.* 38 (7): 883–896. https://doi.org/10.1016/j.compgeo.2011.06.003.

BSI (British Standards Institution). 2010. *Code of practice for strengthened/reinforced soil and other fills.* BS 8006-1. London: BSI.

BSI (British Standards Institution). 2016. *Code of practice for strengthened/reinforced soil and other fills.* BS 8006-1:2010+A1: 2016. London: BSI.

© ASCE   04020126-12   J. Geotech. Geoenviron. Eng.

J. Geotech. Geoenviron. Eng., 2020, 146(11): 04020126

Chai, J. C., S. Shrestha, T. Hino, and T. Uchikoshi. 2017. "Predicting bending failure of CDM columns under embankment loading." *Comput. Geotech.* 91 (Nov): 169–178. https://doi.org/10.1016/j.compgeo.2017.07.015.

Chen, R. P., Y. W. Wang, X. W. Ye, X. C. Bian, and X. P. Dong. 2016. "Tensile force of geogrids embedded in pile-supported reinforced embankment: A full-scale experimental study." *Geotext. Geomembr.* 44 (2): 157–169. https://doi.org/10.1016/j.geotexmem.2015.08.001.

DGGT (Deutsche Gesellschaft für Geotechnik). 2012. *Recommendations for design and analysis of earth structures using geosynthetic reinforcements—EBGEO*. New York: Wiley.

Farag, G. S. F. 2008. "Lateral spreading in basal reinforced embankments supported by pile-like elements." Ph.D. dissertation, Institut für Geotechnik und Geohydraulik, Univ. of Kassel.

Han, J., and M. A. Gabr. 2002. "Numerical analysis of geosynthetic-reinforced and pile-supported earth platforms over soft soil." *J. Geotech. Geoenviron. Eng.* 128 (1): 44–53. https://doi.org/10.1061/(ASCE)1090-0241(2002)128:1(44).

Holmberg, S. 1978. "Bridge approaches on soft clay supported by embankment piles." *Geotech. Eng.* 10 (1): 77–89.

Huang, J., and J. Han. 2009. "3D coupled mechanical and hydraulic modeling of a geosynthetic-reinforced deep mixed column-supported embankment." *Geotext. Geomembr.* 27 (4): 272–280. https://doi.org/10.1016/j.geotexmem.2009.01.001.

Huang, J., and J. Han. 2010. "Two-dimensional parametric study of geosynthetic-reinforced column-supported embankments by coupled hydraulic and mechanical modeling." *Comput. Geotech.* 37 (5): 638–648. https://doi.org/10.1016/j.compgeo.2010.04.002.

Huang, Z. 2019. "Lateral spreading mechanics of column-supported embankments." Ph.D. dissertation, Dept. of Civil and Environmental Engineering, Virginia Polytechnic Institute and State Univ.

Huang, Z., K. Ziotopoulou, and G. M. Filz. 2018. "Numerical predictions of deformations in geosynthetic-reinforced column-supported embankments: Validation of manual dissipation of excess pore pressure approach for undrained and drained analyses." In Vol. 296 of *Proc., IFCEE 2018: Innovations in Ground Improvement for Soils, Pavements, and Subgrades*, 327–336. Reston, VA: ASCE.

Huang, Z., K. Ziotopoulou, and G. M. Filz. 2019. "3D numerical limiting case analyses of lateral spreading in a column-supported embankment." *J. Geotech. Geoenviron. Eng.* 145 (11): 04019096. https://doi.org/10.1061/(ASCE)GT.1943-5606.0002162.

Huang, Z., K. Ziotopoulou, and G. M. Filz. 2020. "Lateral thrust distribution in column-supported embankments: A parametric study via 3D simulations." In *Proc., ASCE Geo-Congress 2020*. Reston, VA: ASCE. https://ascelibrary.org/doi/10.1061/9780784482797.012.

Itasca. 2013. *Structural elements*. Minneapolis, MN: Itasca Consulting Group.

Jamsawang, P., N. Yoobanpot, N. Thanasisathit, P. Voottipruex, and P. Jongpradist. 2016. "Three-dimensional numerical analysis of a DCM column-supported highway embankment." *Comput. Geotech.* 72 (Feb): 42–56. https://doi.org/10.1016/j.compgeo.2015.11.006.

Jenck, O., D. Dias, and R. Kastner. 2009. "Three-dimensional numerical modeling of a piled embankment." *Int. J. Geomech.* 9 (3): 102–112. https://doi.org/10.1061/(ASCE)1532-3641(2009)9:3(102).

Jennings, K., and P. J. Naughton. 2011. "Lateral deformation under the side slopes of piled embankments." In *Proc., Geo-Frontiers 2011*, 142–151. Reston, VA: ASCE. https://ascelibrary.org/doi/10.1061/41165%28397%2916.

Lai, Y., D. Bergado, G. Lorenzo, and T. Duangchan. 2006. "Full-scale reinforced embankment on deep jet mixing improved ground." *Proc. Inst. Civ. Eng. Ground Improv.* 10 (4): 153–164. https://doi.org/10.1680/grim.2006.10.4.153.

Liu, H., C. W. Ng, and K. Fei. 2007. "Performance of a geogrid-reinforced and pile-supported highway embankment over soft clay: Case study." *J. Geotech. Geoenviron. Eng.* 133 (12): 1483–1493. https://doi.org/10.1061/(ASCE)1090-0241(2007)133:12(1483).

Liu, K. W., and R. K. Rowe. 2016. "Performance of reinforced, DMM column-supported embankment considering reinforcement viscosity and subsoil's decreasing hydraulic conductivity." *Comput. Geotech.* 71 (Jan): 147–158. https://doi.org/10.1016/j.compgeo.2015.09.006.

Mahdavi, H., B. Fatahi, H. Khabbaz, M. Krzeminski, R. Santos, and M. Marix-Evans. 2016. "Three-dimensional simulation of a load transfer mechanism for frictional and end bearing CMC supported embankments on soft soil." In *Proc., Geo-China 2016 Advances in Pavement Engineering and Ground Improvement*, 60–67. Reston, VA: ASCE.

McGuire, M. P. 2011. "Critical height and surface deformation of column-supported embankments." Ph.D. dissertation, Dept. of Civil and Environmental Engineering, Virginia Polytechnic Institute and State Univ.

Nunez, M. A., L. Briançon, and D. Dias. 2013. "Analyses of a pile-supported embankment over soft clay: Full-scale experiment, analytical and numerical approaches." *Eng. Geol.* 153 (Feb): 53–67. https://doi.org/10.1016/j.enggeo.2012.11.006.

Pul, S., A. Ghaffari, E. Öztekin, M. Hüsem, and S. Demir. 2017. "Experimental determination of cohesion and internal friction angle on conventional concretes." *ACI Mater. J.* 114 (3): 407–416. https://doi.org/10.14359/51689676.

Reid, W. M., and N. W. Buchanan. 1984. "Bridge approach support piling." *Piling and ground treatment*, 267–274. London: Thomas Telford.

Rowe, R. K., and K.-W. Liu. 2015. "Three-dimensional finite element modelling of a full-scale geosynthetic-reinforced, pile-supported embankment." *Can. Geotech. J.* 52 (12): 2041–2054. https://doi.org/10.1139/cgj-2014-0506.

Schädlich, B., and H. Schweiger. 2014. *Internal report shotcrete model: Implementation validation and application of the shotcrete model*. Delft, Netherlands: Plaxis.

Schaefer, V. R., R. R. Berg, J. G. Collin, B. R. Christopher, J. A. DiMaggio, G. M. Filz, D. A. Bruce, and D. Ayala. 2017. *Ground modification methods reference manual—Volume II*. Washington, DC: FHWA.

Shrestha, S., J. C. Chai, D. T. Bergado, T. Hino, and Y. Kamo. 2015. "3D FEM investigation on bending failure mechanism of column inclusion under embankment load." *Lowland Technol. Int.* 17 (3): 157–166. https://doi.org/10.14247/lti.17.3_157.

Sloan, J. A. 2011. "Column-supported embankments: Full-scale tests and design recommendations." Ph.D. dissertation, Dept. of Civil and Environmental Engineering, Virginia Tech.

Sloan, J. A., G. M. Filz, J. G. Collin, and P. Kumar. 2014. *Column-supported embankments: Field tests and design recommendations*. 2nd ed. Blacksburg, VA: Center for Geotechnical Practice and Research, Virginia Tech.

Stewart, M. E., M. P. Navin, and G. M. Filz. 2004. "Analysis of a column-supported test embankment at the I-95/route 1 interchange." In *Geotechnical engineering for transportation projects*. Reston, VA: ASCE. https://ascelibrary.org/doi/abs/10.1061/40744%28154%29123.

van Eekelen, S. J. M., and M. H. A. Brugman. 2016. *Design guideline basal reinforced piled embankments*. Boca Raton, FL: CRC Press.

Yapage, N. N. S., and D. S. Liyanapathirana. 2014. "A parametric study of geosynthetic-reinforced column-supported embankments." *Geosynthetics Int.* 21 (3): 213–232. https://doi.org/10.1680/gein.14.00010.

Yapage, N. N. S., D. S. Liyanapathirana, R. B. Kelly, H. G. Poulos, and C. J. Leo. 2014. "Numerical modeling of an embankment over soft ground improved with deep cement mixed columns: Case history." *J. Geotech. Geoenviron. Eng.* 140 (11): 04014062. https://doi.org/10.1061/(ASCE)GT.1943-5606.0001165.

Ye, G., Y. Cai, and Z. Zhang. 2016. "Numerical study on load transfer effect of Stiffened Deep Mixed column-supported embankment over soft soil." *KSCE J. Civ. Eng.* 21 (3): 703–714. https://doi.org/10.1007/s12205-016-0637-8.

Yu, Y., R. J. Bathurst, and I. P. Damians. 2016. "Modified unit cell approach for modelling geosynthetic-reinforced column-supported embankments." *Geotext. Geomembr.* 44 (3): 332–343. https://doi.org/10.1016/j.geotexmem.2016.01.003.

Zheng, J. J., B. G. Chen, Y. E. Lu, S. W. Abusharar, and J. H. Yin. 2009. "The performance of an embankment on soft ground reinforced with geosynthetics and pile walls." *Geosynthetics Int.* 16 (3): 173–182. https://doi.org/10.1680/gein.2009.16.3.173.

© ASCE 04020126-13 J. Geotech. Geoenviron. Eng.

J. Geotech. Geoenviron. Eng., 2020, 146(11): 04020126

Zhuang, Y., and K. Y. Wang. 2015. "Three-dimensional behavior of biaxial geogrid in a piled embankment: Numerical investigation." *Can. Geotech. J.* 52 (10): 1629–1635. https://doi.org/10.1139/cgj-2014 -0538.

Zhuang, Y., and K. Y. Wang. 2016. "Finite-element analysis on the effect of subsoil in reinforced piled embankments and comparison with theoretical method predictions." *Int. J. Geomech.* 16 (5): 04016011. https://doi .org/10.1061/(ASCE)GM.1943-5622.0000628.

© ASCE 04020126-14 J. Geotech. Geoenviron. Eng.

J. Geotech. Geoenviron. Eng., 2020, 146(11): 04020126